Trimodal color-fluorescence-polarization endoscopy aided by a tumor selective molecular probe accurately detects flat lesions in colitis-associated cancer

Tauseef Charanya
Timothy York
Sharon Bloch
Gail Sudlow
Kexian Liang
Missael Garcia
Walter J. Akers
Deborah Rubin
Viktor Gruev
Samuel Achilefu

SPIE.

Trimodal color-fluorescence-polarization endoscopy aided by a tumor selective molecular probe accurately detects flat lesions in colitis-associated cancer

Tauseef Charanya,[a,b] Timothy York,[c] Sharon Bloch,[a] Gail Sudlow,[a] Kexian Liang,[a] Missael Garcia,[c] Walter J. Akers,[a] Deborah Rubin,[d] Viktor Gruev,[c] and Samuel Achilefu[a,b,e,*]

[a]Washington University in St. Louis, Department of Radiology, 4525 Scott Avenue, East Building, St. Louis, Missouri 63110, United States
[b]Washington University in St. Louis, Department of Biomedical Engineering, 1 Brookings Drive, St. Louis, Missouri 63110, United States
[c]Washington University in St. Louis, Department of Computer Science and Engineering, 1 Brookings Drive, St. Louis, Missouri 63110, United States
[d]Washington University in St. Louis, Department of Medicine, 660 South Euclid Avenue, St. Louis, Missouri 63110, United States
[e]Washington University in St. Louis, Department of Biochemistry and Molecular Biophysics, 660 South Euclid Avenue, St. Louis, Missouri 63110, United States

Abstract. Colitis-associated cancer (CAC) arises from premalignant flat lesions of the colon, which are difficult to detect with current endoscopic screening approaches. We have developed a complementary fluorescence and polarization reporting strategy that combines the unique biochemical and physical properties of dysplasia and cancer for real-time detection of these lesions. Using azoxymethane-dextran sodium sulfate (AOM-DSS) treated mice, which recapitulates human CAC and dysplasia, we show that an octapeptide labeled with a near-infrared (NIR) fluorescent dye selectively identified all precancerous and cancerous lesions. A new thermoresponsive sol-gel formulation allowed topical application of the molecular probe during endoscopy. This method yielded high contrast-to-noise ratios (CNR) between adenomatous tumors (20.6 ± 1.65) and flat lesions (12.1 ± 1.03) and surrounding uninvolved colon tissue versus CNR of inflamed tissues (1.62 ± 0.41). Incorporation of nano-wire-filtered polarization imaging into NIR fluorescence endoscopy shows a high depolarization contrast in both adenomatous tumors and flat lesions in CAC, reflecting compromised structural integrity of these tissues. Together, the real-time polarization imaging provides real-time validation of suspicious colon tissue highlighted by molecular fluorescence endoscopy. © *The Authors. Published by SPIE under a Creative Commons Attribution 3.0 Unported License. Distribution or reproduction of this work in whole or in part requires full attribution of the original publication, including its DOI.* [DOI: 10.1117/1.JBO.19.12.126002]

1 Introduction

Inflammatory bowel diseases (IBDs) consist of ulcerative colitis and Crohn's disease, which are characterized by uncontrolled inflammation of the gastrointestinal tract in genetically susceptible individuals exposed to environmental risk factors.[1] The incidence and prevalence of IBD has increased in recent years, affecting 1.4 million Americans in 2012 alone.[2] Moreover, the peak onset of this disease occurs in the second and third decades of life, subjecting these patients to a twofold or greater lifetime risk of developing colorectal cancer (CRC) than normal subjects.[2] A meta-analysis of colorectal cancer risk suggests a cumulative incidence of malignancy of 2% by 10 years, 8% by 20 years, and 18% by 30 years postdiagnosis.[1] Sporadic CRC and colitis-associated cancer (CAC) together account for 52,000 mortalities every year in the United States alone, making them the second leading causes of death from cancer among adults.[3]

Unlike sporadic CRC, which develops from an adenomatous polyp, CAC follows a dysplasia-carcinoma sequence where the inflamed mucosa gives rise to flat and polypoid dysplasia that lead to invasive cancers.[4,5] The lack of elevated growth component as in polyps creates an enormous challenge in detecting these flat lesions during surveillance colonoscopy. For example, 50% to 80% of the lesions that are missed during surveillance colonoscopy are flat.[6,7] Several murine models have been developed to recapitulate human CAC.[8] In particular, the azoxymethane-dextran sodium sulfate (AOM-DSS) model has been used to demonstrate that advanced cancers develop from flat lesions without transitioning through a polypoid intermediate.[9] Although dysplasia could serve as a marker for malignancy in colitis patients, current surveillance protocols fail to reliably identify early stages of CAC.[10]

Recent advances in biomarker and imaging platforms have focused on either morphological or molecular features of these flat lesions, neither of which is sufficient to aid the diagnosis of these pathologies in real time during colonoscopy. Efforts to identify polyps and cancerous lesions using chromoendoscopy, virtual chromoendoscopy, narrow-band imaging, and postprocessing algorithms such as i-SCAN and FICE have failed to reliably delineate flat lesions from surrounding uninvolved tissue.[11–14] In particular, chromoendoscopy is currently recommended for routine surveillance of IBD patients. Although

---

*Address all correspondence to: Samuel Achilefu, E-mail: achilefus@mir.wustl.edu

this technique has improved the detection rates of flat lesions from 28% to 56%,[15] the fraction of undetected lesions remains unsatisfactory. Similarly, optical coherence tomography has been used to differentiate diseased from normal esophageal tissue, but the inhomogeneous backscattering of signal in high-grade dysplasia limits the diagnostic information derived from this approach.[16,17] To improve detection sensitivity, newer fluorescence endoscopic techniques, such as confocal laser endomicroscopy, have been developed. In conjunction with fluorescence contrast agents, these techniques allow visualization of molecular signatures of cancer, but lack a real-time validation strategy and provide only a limited field of view (FOV).[18–20]

The overarching goal for this study is to develop and to validate a tri-modal endoscopic system consisting of fluorescence, polarization, and color modules for colonoscopy. The color imaging module provides conventional visual feedback of the anatomical structures of tissue. Utilizing a near-infrared (NIR) fluorescent molecular reporter of flat lesions, the fluorescence module highlights underlying pathologies that are not visible by conventional color imaging methods. Complementary polarization signal highlights tissue that is largely opaque to both fluorescence and color modules,

thereby facilitating full characterization and instant cross-validation of suspicious lesions. An unprecedented high sensitivity and specificity approaching 100% were obtained by combining these three imaging modalities.

2 Materials and Methods

2.1 *Using Unpolarized Light for Polarization Endoscopy*

Both incident and reflected light are fully described by the Stokes vectors, which contain four parameters; S_0, S_1, S_2, and S_3. The first Stokes parameter, S_0, describes the intensity of the light; the second Stokes parameter, S_1, describes the difference between horizontally and vertically polarized light; the third Stokes parameter, S_2, describes the difference between 45 and 135-degree polarized light; and the fourth Stokes parameter, S_3, describes the difference between left and right circularly polarized light. The polarization of light changes upon reflection from a surface, with the change based on the reflection geometry and the medium and surface materials. The Mueller matrix in Eq. (1) mathematically describes the change in polarization for a reflection from a tissue,

$$M_{\mathrm{ref}} = \frac{1}{2}\left(\frac{\tan \Theta_x}{\sin \Theta_y}\right)^2 \begin{bmatrix} \cos^2 \Theta_x + \cos^2 \Theta_y & \cos^2 \Theta_x - \cos^2 \Theta_y & 0 & 0 \\ \cos^2 \Theta_x - \cos^2 \Theta_y & \cos^2 \Theta_x + \cos^2 \Theta_y & 0 & 0 \\ 0 & 0 & -2 \cos \Theta_x \Theta_y & 0 \\ 0 & 0 & 0 & -2 \cos \Theta_x \Theta_y \end{bmatrix}, \tag{1}$$

where Θ_x is the difference in the incident and refracted angles ($\Theta_x = \theta_i - \theta_r$), and Θ_y is the sum of the incident and refracted angles ($\Theta_y = \theta_i + \theta_r$). Snell's law [Eq. (2)] relates the incident and refracted angles

$$n_1 \sin \theta_1 = n_2 \sin \theta_r, \tag{2}$$

where θ_i is the incident angle, θ_r is the refracted angle, and n_1 and n_2 are the indices of the media and object, respectfully. Multiplying the incident Stokes vector with the Mueller matrix for reflection [Eq. (3)] results in the Stokes vector for light reflected off the surface.

$$\begin{bmatrix} S_0 \\ S_1 \\ S_2 \\ S_3 \end{bmatrix}_{\mathrm{REF}} = M_{\mathrm{ref}} \begin{bmatrix} S_0 \\ S_1 \\ S_2 \\ S_3 \end{bmatrix}_{\mathrm{INPUT}}. \tag{3}$$

The reflected Stokes vector contains all the information needed to compute the degree of linear polarization (DoLP) for the reflected light [Eq. (4)]. The DoLP measures how linearly polarized the light becomes after reflection, from 0 (non-linear polarization) to 1 (completely linearly polarized).

$$\mathrm{DoLP_{REF}} = \frac{\sqrt{S_{1,\mathrm{REF}}^2 + S_{2,\mathrm{REF}}^2}}{S_{0,\mathrm{REF}}}. \tag{4}$$

The angle of polarization (AoP) measures the orientation of the reflected light with respect to the detector, and is computed from S_1 and S_2 [Eq. (5)].

$$\mathrm{AoP_{REF}} = \frac{1}{2} \arctan\left(\frac{S_{2,\mathrm{REF}}}{S_{1,\mathrm{REF}}}\right). \tag{5}$$

If the input Stokes vector is unpolarized light [1, 0, 0, 0], the DoLP of the reflected light becomes [Eq. (6)]

$$\mathrm{DoLP_{REF}} = \frac{\cos^2 \Theta_x - \cos^2 \Theta_y}{\cos^2 \Theta_x + \cos^2 \Theta_y}, \tag{6}$$

and the reflected AoP is zero, as the reflected S_2 component is zero. This applies only to a planar reflection. On a three-dimensional surface, the azimuthal angle is modeled as a rotation of the axis of the planar reflection of a microfacet of the surface into the axis of the sensor by a rotation angle ϕ. Using the Mueller matrix of a rotation [Eq. (7)],

$$M_{\mathrm{rot}}(2\phi) = \begin{bmatrix} 1 & 0 & 0 & 0 \\ 0 & \cos 2\phi & \sin 2\phi & 0 \\ 0 & -\sin 2\phi & \cos 2\phi & 0 \\ 0 & 0 & 0 & 1 \end{bmatrix}, \tag{7}$$

the reflection equation becomes [Eq. (8)]

$$\begin{bmatrix} S_0 \\ S_1 \\ S_2 \\ S_3 \end{bmatrix}_{\mathrm{REF}} = M_{\mathrm{rot}}(-2\phi) M_{\mathrm{ref}} M_{\mathrm{rot}}(2\phi) \begin{bmatrix} S_0 \\ S_1 \\ S_2 \\ S_3 \end{bmatrix}_{\mathrm{INPUT}}. \tag{8}$$

The reflected DoLP remains unchanged; however, the AOP becomes equal to the amount of curvature [Eq. (9)].

$$\text{AOP} = \frac{1}{2}\arctan\left[\frac{\frac{1}{4}(\cos^2\Theta_x - \cos^2\Theta_y)\csc^2\Theta_y \sin 2\phi \tan^2\Theta_x}{\frac{1}{4}(\cos^2\Theta_x - \cos^2\Theta_y)\csc^2\Theta_y \cos 2\phi \tan^2\Theta_x}\right]$$

$$= \frac{1}{2}\arctan\left(\frac{\sin 2\phi}{\cos 2\phi}\right) = \phi,$$

$$\text{DOLP} = \frac{4n_2\sin^2(\theta_i)\cos(\theta_i)\sqrt{1 - \frac{\sin^2(\theta_i)}{n_2^2}}}{n_2 2\cos(2\theta_i) + 2\sin^4\theta_i - 2\sin^2\theta_i\cos^2\theta_i + n_2^2}. \quad (9)$$

2.2 Synthesis of Polarization Filter

The fabrication of the nanowire polarization filter was conducted at the fabrication facilities at Washington University in St. Louis in collaboration with Moxtek Inc. (Orem, UT). The nanofabrication of the optical nanowire polarization filter was achieved by first depositing a 70-nm thin film of aluminum, followed by a 30-nm thin film deposition of SiO_2 using e-beam evaporation. A 100-nm thin layer of photoresist S-1805 was spun coated at 3000 rpm and baked at 115°C for 60 s. A continuous-wave (CW) single frequency Nd:YAQ laser with a 532-nm wavelength was used together with a frequency doubler to produce coherent light waves at a 266-nm wavelength. Two CW 266-nm wavelengths were aligned to interfere at 110 deg and produce an interference pattern with a period of 140 nm. The

interference pattern was transferred to the photoresist by exposing the sample for 40 s. After developing the photoresist, the pattern was transferred to the SiO_2 using the standard RIE/ICP etching recipe for SiO_2. The SiO_2 was used as a hard mask for etching the aluminum. The aluminum was etched for 150 s using 30 sccm BCl_3, 15 sccm Cl_2, 10-mTorr pressure, 70°C temperature, 100-W RIE power, and 150-W ICP power. The procedure was repeated four times and the sample was rotated by 45 deg each time to produce nanowires with four different orientations. The nanowire polarization filters were flip-chip bonded to a commercially available charge-coupled device (CCD) imaging sensor (Kodak KAI 2020).

2.3 Fluorescence and Polarization Endoscope

The new endoscopic device shown in Fig. 1(a) is capable of imaging in three different modes: RGB, fluorescence, and polarization. In the RGB mode, an endoscopic cold light fountain (Xenon Nova 175; Karl Storz, Tuttlingen, Germany) with adjustable light intensity was used as the light source. The light cable was coupled to the illumination channel on a 0 deg Hopkins (1.9 mm × 10 cm) straightforward telescope (Karl Storz, Tuttlingen, Germany), as shown in Fig. 1(a). Images were captured by an NIR-sensitive CCD camera (Fluorvivo; INDEC Biosystems) with an RGB Bayer filter. A telescope
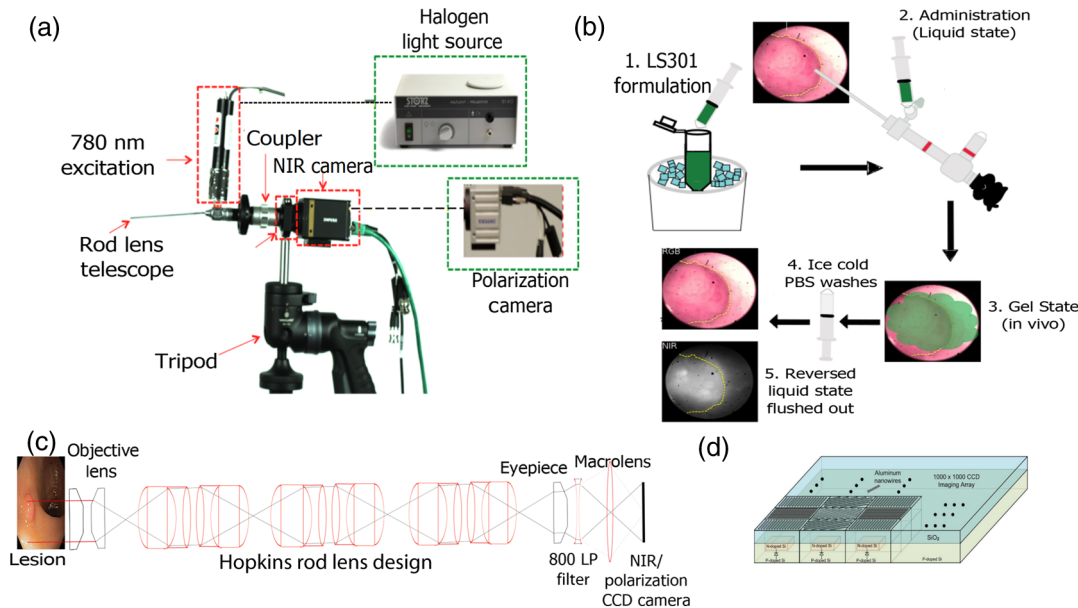

Fig. 1 Trimodal color-fluorescence-polarization endoscopy utilizing a novel molecular probe administration approach. (a) Endoscope setup used to perform white light, fluorescence, and polarization endoscopy. A telescope coupler with a focus ring was used to focus the image onto the image formation plane located at the back of the Karl Storz telescope lens. For white light endoscopy, Xenon Nova 175 was used as a light source and a charge-coupled device (CCD) camera (Fluorvivo) with an RGB Bayer filter was used. In near-infrared (NIR)- fluorescence mode, a 100-mW 780-nm laser excitation source (inset I) was coupled to the light source channel on the endoscope. An 800-nm long-pass emission filter was placed behind the telescope, as shown in the figure. A CCD camera with NIR capabilities (Fluorvivo) was utilized to capture images in NIR-fluorescence mode. In polarization mode, the Xenon broadband light source was used along with a custom-made polarization camera, as shown in inset II. The entire setup was fixed on a tripod and an x-y translation stage was utilized for finer adjustments to avoid causing damage to the walls of the colon. (b) Steps involved in the dye administration method utilizing Pluronic F127 gel formulation. (c) Schematic of the light path associated with the endoscopy setup presented in (a). (d) Polarization sensor consisting of an imaging array arranged in blocks of four (two by two) superpixels. Each superpixel consists of four pixels that are composed of nanowire polarization filters with the transmission axis oriented at 0 deg, 45 deg, 90 deg, and 135 deg. These nanowires are 70-nm wide, 140-nm tall, and spaced 140 nm from center to center.

coupler with a focus ring (Karl Storz, Tuttlingen, Germany) focused the CCD camera on the image formation plane at the back of the telescope.

In the fluorescence mode, the cold light fountain source was replaced by a 100 mW, 780-nm excitation source (Lasermax, New York, USA). An 800-nm long-pass emission filter (ThorLabs, Newton, New Jersey) was placed behind the telescope in a slit of a custom-made adapter designed to couple the macro lens to the telescope. Images were captured using the Fluorvivo CCD camera equipped with a Sony ICX285 sensor (quantum efficiency of 30% at 800 nm).

In the polarization mode, the same endoscopic cold light fountain used as the light source for the RGB imaging was utilized here. Images were captured using the camera housing the polarization sensor described earlier.

2.4 Polarization Endoscopy Calibration

Since the endoscope is composed of a series of optical elements, the polarization state of the input light can be modified as the light travels through the endoscope. Every optical element in the endoscope will perturb the Stokes vector of the incident light and these perturbations need to be carefully examined to ensure that the endoscope preserves the polarization signatures of the incident light. We created an optical setup to evaluate the polarization properties of the endoscope as depicted in Fig. 2(a). The setup is composed of a polarization state generator and a polarization state analyzer.

The polarization state analyzer for the light emerging from the endoscope is measured using a division of time polarimeter. The polarimeter is composed of a zero-order precision wave plate (Newport 20RP34-514.5) with a quarter wave retardance at 514.5 nm, a precision linear polarizer (Newport 20LP-VIS-B) with a wavelength range of 400 to 700 nm, and a USB controlled optical power meter (Thorlabs PM100D) with a visible spectrum calibrated photodiode (Thorlabs S120 V). This instrument quantifies the Stokes vector as described by Eqs. (10) through (13):[21]

$$S_0 = \frac{1}{2}[I(0 \ \text{deg}, 0 \ \text{deg}) + I(45 \ \text{deg}, 0 \ \text{deg})$$
$$+ I(90 \ \text{deg}, 0 \ \text{deg}) + I(135 \ \text{deg}, 0 \ \text{deg})], \qquad (10)$$
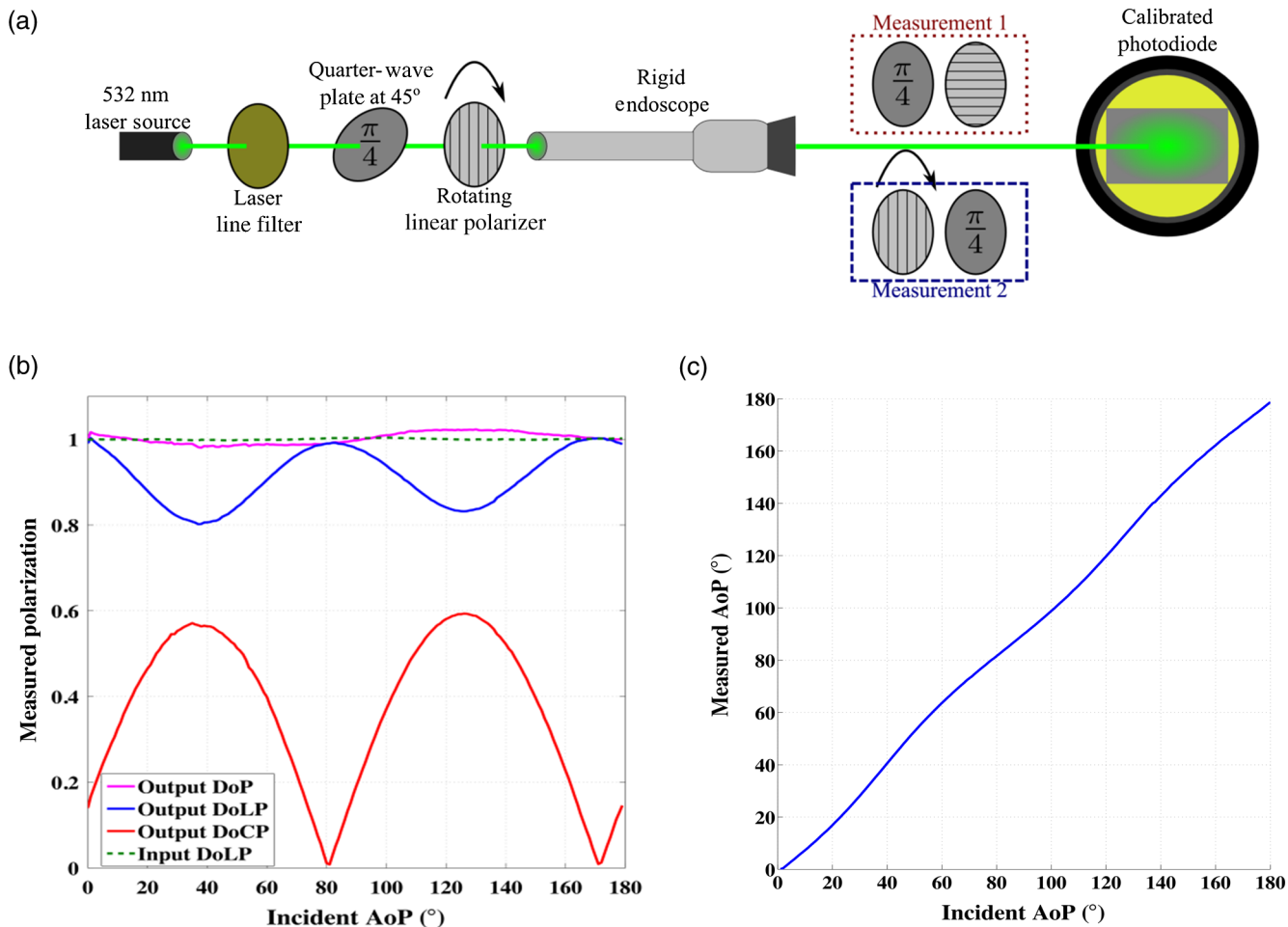

Fig. 2 Optical setup and characterizations involved for evaluating the performance of the endoscope. (a) A polarization state generator is used to illuminate the endoscope and a polarization state analyzer is used to evaluate the polarization performance of the endoscope. (b) Measurements of the polarization performance of the endoscope. The endoscope is illuminated with linearly polarized light between 0 and 180 deg. While the DoLP decreases by ∼20% due to retarder elements in the endoscope, degree of polarization remains at 100%, indicating involvement of circular polarization component. (c) Measured angle of polarization for the light emerging from the endoscope. The endoscope is illuminated with linearly polarized light between 0 and 180 deg. The endoscope does not affect the angle of polarization of the incident light.

$$S_1 = I(0 \text{ deg}, 0 \text{ deg}) - I(90 \text{ deg}, 0 \text{ deg}), \qquad (11)$$

$$S_2 = I(45 \text{ deg}, 0 \text{ deg}) - I(135 \text{ deg}, 0 \text{ deg}), \qquad (12)$$

$$S_3 = S_0 - 2I(45 \text{ deg}, 90 \text{ deg}). \qquad (13)$$

In these equations, $I(\theta, \phi)$ is the intensity of the optical beam, θ describes the linear polarizer transmission axis angle in degrees, and ϕ describes the wave plate retardance, which is 90 deg for the wave plates. To measure (45 deg, 90 deg), the light beam passes through a waveplate with the fast axis along the x-axis and then through a linear polarizer with transmission axis rotated at 45 deg; to measure $I(\theta, 0)$, the beam passes through a linear polarizer with its transmission axis rotated θ deg and then through a wave plate with its fast axis along the x-axis. Hence, all measurements are done with both a linear polarization filter and a quarter wave plate to take any optical losses that can occur in either optical element into account.

2.5 Formulation of LS301

The NIR dye LS301, which was previously reported,[22] was synthesized in our lab via modification of a previously described method.[23] LS301 consists of a NIR fluorescent dye, cypate (780 ex/830 em), and a cyclic peptide sequence, D-Cys-Gly-Arg-Asp-Ser-Pro-Cys-Lys (c(DCGRDSPC)K). Figure 3(a)

shows the molecular structure, absorption, and emission spectra of LS301.

To formulate LS301 in a sol-gel mixture for topical administration, Pluronic F-127 (1 g; Sigma Aldrich, St. Louis, MO) was dissolved in phosphate buffered saline (PBS) (10 mL; PBS) to obtain a 10% (w/v) stock solution. A solution of LS301 (0.5 mL; 60 μM) was dissolved in 10% w/v aqueous Pluronic solution to form the sol-gel system, which was stored on ice prior to administration to maintain its liquid state.

2.6 In Vivo Small Animal Endoscopy

Mice were anesthetized via intraperitoneal injection of a solution of ketamine (85 mg/kg) and xylazine (15 mg/kg). They were then placed supine on a z-translation stage prior to the procedure. To avoid unnecessary movements of the endoscope during mode switches and to assess a region of interest within the same FOV, the imaging setup was immobilized on a tripod. To obtain 1-mm translation inside the colon, the endoscope was set on an x-y translation stage. The rigid endoscope could reach as far as 4 cm into the mouse colon, at which point it encountered the splenic flexure.

Prior to topical administration of the LS301 solution, the mouse colon was rinsed with PBS to remove debris and mucous. A novel administration technique enabled interaction of the mouse tissue with our molecular agent for a longer incubation time than would otherwise be achievable. A cold solution of the LS301 in Pluronic F127 sol-gel (0.5 mL) was carefully injected
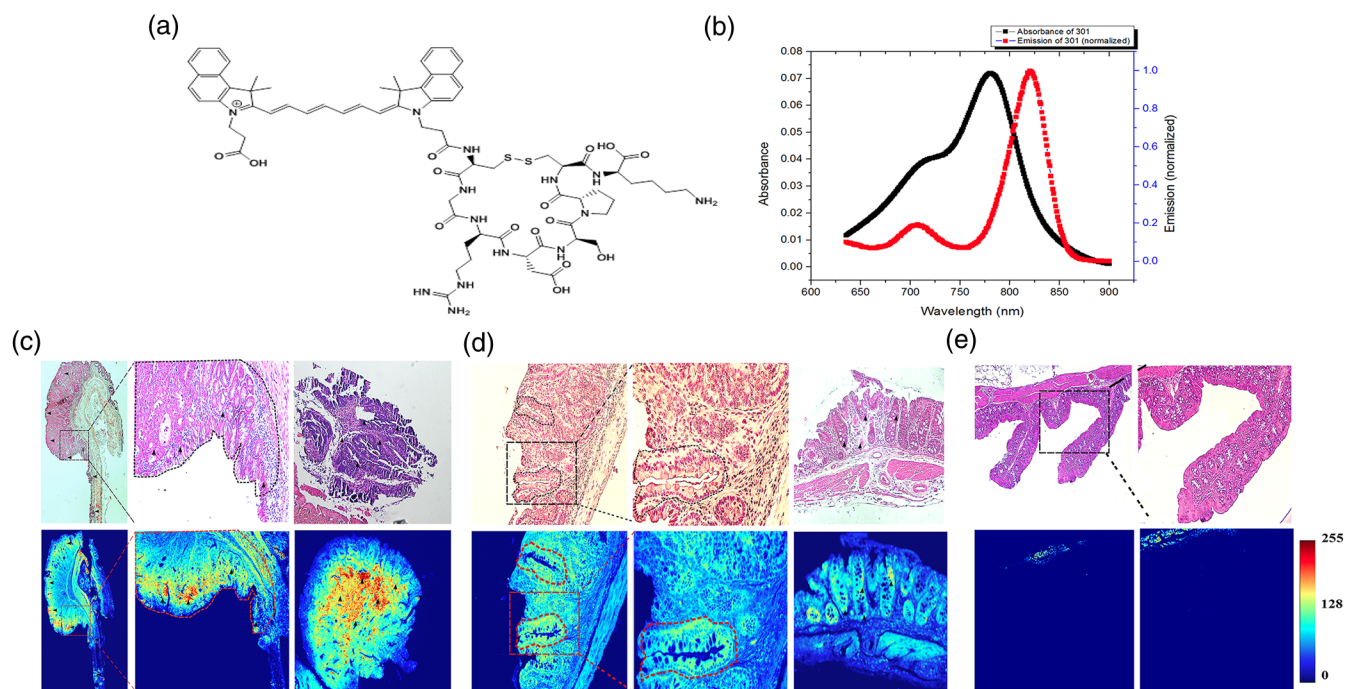

Fig. 3 *Ex-vivo* fluorescence imaging using LS301 on azoxymethane-dextran sodium sulfate (AOM-DSS) tissue sections. (a) Molecular structure of LS301. (b) Absorption and emission spectra of LS301. (c) H&E and corresponding NIR fluorescence stains of tumors identified along the distal colon of a mouse treated with AOM-DSS. Arrow points the regions of the tumor that exhibit enhanced binding of LS301. Black and red dotted lines identify the region that marks the initiation of adenomatous tumor. (d) H&E and corresponding NIR fluorescence stains of dysplastic lesions identified along the colon of mice treated with AOM-DSS. Regions marked by red dotted lines mark the boundaries of the crypts. Arrows point to regions along the aberrant crypts toward which LS301 demonstrates preferential binding. (e) H&E and corresponding NIR fluorescence stains of normal ascending colon of mice treated with AOM-DSS displaying minimal nonspecific probe binding toward muscularis mucosa.

via the examination sheath of the endoscope. The solution turned into a gel instantaneously along the distal colon. After 10 min of incubation, cold PBS was flushed through the examination sheath to reverse the gel into a liquid state. After thorough rinsing of the colon with 3 to 5 PBS washes, fluorescence and polarization endoscopy were performed. Steps involved in this process are illustrated in Fig. 1(b).

2.7 *In Situ Fluorescence-Polarization Imaging*

Postendoscopy mice were sacrificed and the distal colon was isolated from the peritoneum without dislodging it from the animal to locate tumors that were identified during fluorescence-polarization endoscopy. A 780-nm excitation source illuminated the sample for fluorescence imaging and an 800-nm long-pass filter was placed in front of the image capture device. Images were captured with an exposure time of 0.5 s. Polarization imaging was obtained using the system described above.

3 Results

3.1 *Simulating Unpolarized Light in Reflectance Polarization Endoscopy*

3.1.1 *Simulating reflectance imaging using unpolarized light source for polarization endoscopy*

Most polarization methods typically use a polarization filter to illuminate a tissue and an orthogonal polarization filter placed at the detector side to measure polarization contrast information. This imaging modality requires careful optical alignment of the polarization filters and is applicable for microscopy or *ex vivo* imaging. Due to space constraints in an endoscope, polarization contrast imaging is challenging. In this study, we allowed the intrinsic properties of tissue to linearly polarize the incident unpolarized light and backscattering to depolarize the reflected light, which is captured by our polarization sensor as shown in Fig. 4(a). To ensure that this polarization technique is sensitive to differences in tissue properties, simulations using Muller calculus for reflection and Monte Carlo simulations for backscattering were performed (see below) using tissue refractive index values previously reported in the literature. Diseased tissues have a lower refractive index (1.39) than healthy tissues (1.46), thereby serving as an imaging biomarker for the polarization imaging platform. Given the importance of angle of incidence, the DoLP signature arising from healthy and diseased tissues was plotted against the incidence angle using both Frenel's reflectance and Monte Carlo simulations as shown in Fig. 4(b) and an imaging angle of 15 deg for *in vivo* endoscopy. At 15 deg, we obtained ~4% DoLP difference between healthy and diseased tissues, which is sufficient to delineate normal from diseased tissues. While standard endoscopy procedures range in angles of imaging between 15 deg and 35 deg, our *ex vivo* imaging setup utilized a 35 deg angle, which results in a DoLP change of 20% between healthy and diseased tissues according to Fig. 4(b). Based on the differences in tissue refractive indices, radius and density of nuclei, absorption coefficient between healthy and diseased tissues,[24,25] and backscattering of light, we illustrate the propagation of light in the two stages of CAC development: adenomatous polyp and flat, depressed lesions, respectively This simulation demonstrates that the polarization method is capable of cross-validating CAC and associated flat lesions in real time, guided by enhanced fluorescence in pathologic tissue.

3.1.2 *Simulating unpolarized light for polarization endoscopy*

To ensure that this polarization technique is sensitive to differences in tissue properties, simulations using Muller calculus for reflection and Monte Carlo simulations for backscattering were performed. The difference in polarization signatures is due to a combination of Fresnel reflectance and backscattered intensity from the unpolarized source. The incident, unpolarized light becomes partially polarized upon reflection as shown in Fig. 4(a). The partially polarized light mixes with the backscattered intensity from the tissue and further depolarizes the incident light due to the optical parameters of the tissue. Assuming that scattering comes mostly from the nucleus, backscatter is simulated as a dispersion of spheres with optical properties similar to those of the nucleus, performed using the algorithm previously reported.[26] In tumor tissue, scattering comes mostly from the large sized, dense nuclei, whereas in uninvolved tissue, scattering primarily arises from scatterers associated with the mucosa and submucosa regions. Verification is done using polarized Monte Carlo simulation software with a polydisperse set of scatterers drawn from a uniform distribution. In order to simulate the differential optical parameters arising from tumor versus unhealthy tissue, differences in nuclear radii, density of nuclei, index of refraction of nuclei, and absorption coefficient were considered and obtained from the literature.[27–30] Perelman has successfully extracted valuable information about the density and size distribution of mucosal cells and used them as indicators of disease state (neoplastic precancerous changes in biological tissue). Increases in size and density of the nucleus is associated with a later diseased state in these studies. Furthermore, this is supported by Backman et al. The studies conducted illustrate the higher level of backscattered light associated with a denser and larger nuclei concentration. This leads the polarization state of reflected light to be more depolarized when compared to healthy tissue comprising uniformly distributed, less dense, and smaller nuclei.

We took a similar approach in modeling the backscattered intensity as the combination of backscatter from the mucosa added to the backscatter from the submucosa after propagation back through the mucosa.[25] Since the light used was a 6000 K Xenon source, the simulations take place at wavelengths between 400 and 700 nm in 25-nm increments, normalized to the intensity of the bulb at these wavelengths. An increase in backscatter from the tumor tissue effectively depolarizes the Fresnel reflected DoLP, resulting in a lower measured DoLP for tumor when compared to the surrounding uninvolved region.

3.2 *Development of Trimodal Color, Fluorescence, and Polarization Endoscope*

The goal of the instrument development was to retain the features of widely used clinical endoscopes while incorporating new reporting strategies for enhanced diagnosis of endoscope-accessible organs. Toward this goal, we developed a novel endoscope that is capable of presenting imaging data in color (RGB), NIR fluorescence, and polarization modes. Color colonoscopy is the standard of care, while NIR fluorescence and polarization provide new reporting signals for a molecularly targeted imaging agent and tissue pathophysiology, respectively. A detailed description of the endoscopy procedure is available in Sec. 2.6. Briefly, a rigid Hopkins
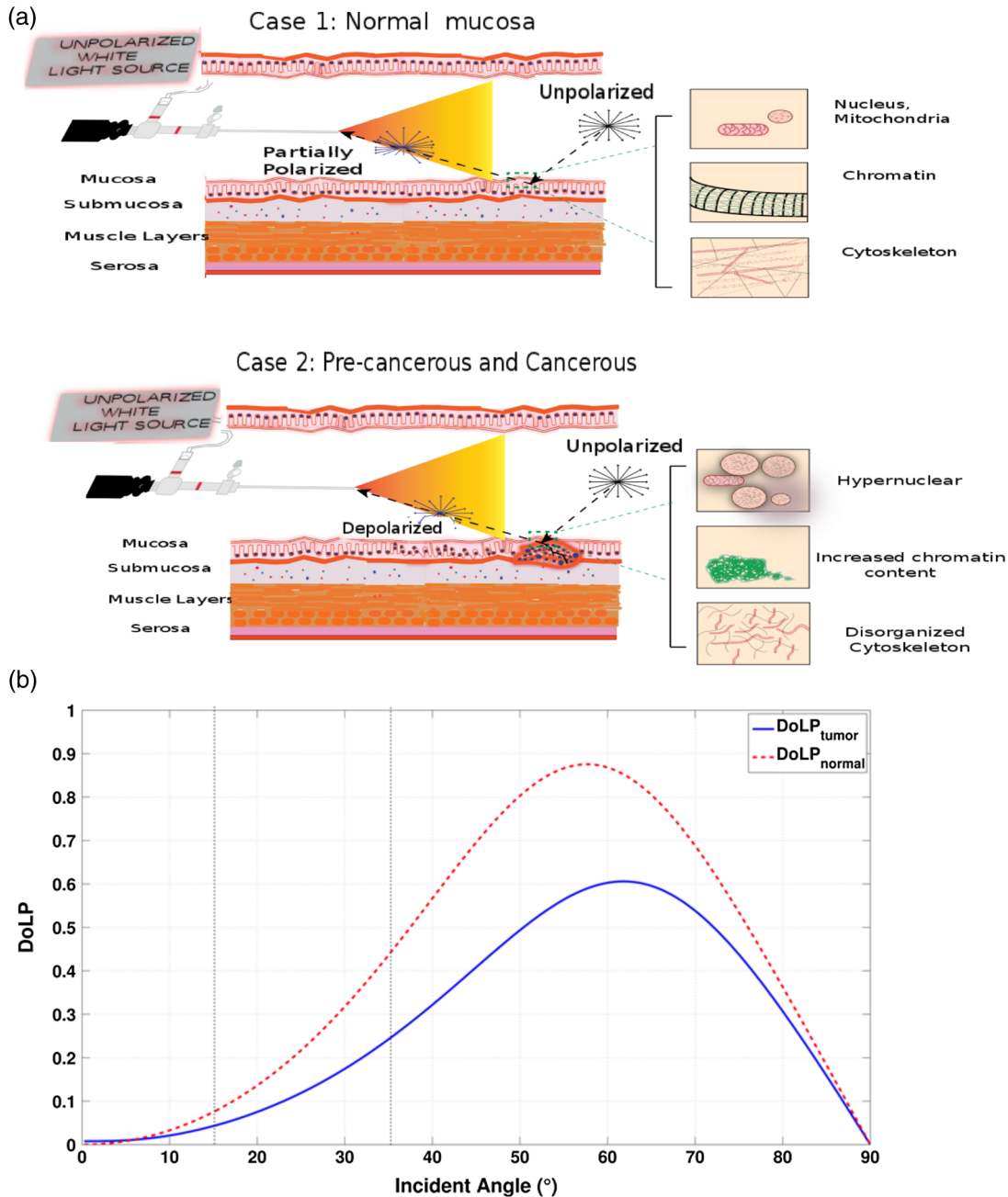
Fig. 4 Concept of reflectance imaging using unpolarized light. (a) Case 1 illustrates the propagation of light in healthy mucosa. Unpolarized light illuminates the region of colon under investigation. Light returning back from the wall of the colon interacts with the healthy mucosa as shown, and obtains partially polarized prior to detection in a tissue composition-dependent manner. Cytoskeletal organized actin fibers partially polarize the light. Case 2 illustrates the propagation of light in a flat, depressed lesion. Unpolarized light reflected from the wall of the colon interacts with pathologic tissue, which depolarizes the light. Larger and denser nuclei serve as source of scatterers in cancer cells, which favor depolarization. (b) A plot of degree of linear polarized (DoLP) light versus incident angle of 0 deg straightforward endoscope. Reflected light from tumor tissue (blue) and healthy tissue (red) is modeled using both Frenel's reflectance and Monte Carlo simulations. Dotted vertical black lines serve as a comparative tool for DoLP signature at 15 deg (*in vivo* studies) and 35 deg (*ex vivo* studies).

endoscope fitted with a Xenon lamp and a 780-nm laser served as RGB/polarization and NIR light sources, respectively, as shown in Figs. 1(a) and 1(b). We used a visible/NIR-sensitive CCD camera with an RGB Bayer filter and 25% quantum efficiency at 800 nm to capture both color and NIR images.

3.2.1 Real-time polarization imaging

To capture the light polarization information, a division of the focal plane polarization imaging sensor was developed, where the incoming light was filtered *via* a polarization filter array consisting of four nanowire polarization filters offset by 45 deg prior

to absorption by a silicon photodiode as shown in Fig. 1(d).[31,32] The amplitude of the filtered light wave was recorded by photodetectors underneath the aluminum nanowire polarization filters. The tissue was illuminated with unpolarized light *via* the light port of a Karl Storz rigid endoscope and the reflected light was collected *via* our custom-built polarization sensor. The polarization state of the reflected light from the tissue was determined by both the relative position of the camera and the index of refraction of the imaged tissue, [Eq. (4)]. The use of an unpolarized light source simplified the imaging setup and allowed the intrinsic morphological and physiological properties of the tissue to dictate the captured polarization signature. This imaging method differs from typical polarization contrast imaging, where linear polarized illumination is used to illuminate a tissue and a detector with cross linear polarization is used to record the reflected light. Due to complex alignment requirements of the polarization filters on both the illumination and detection components, application of traditional polarization contrast imaging is limited for *in vivo* endoscopy.

3.2.2 *Polarization performance of the endoscope: calibration study*

In order to examine how the polarization state of the input light is modified as the light travels through the endoscope, we created an optical setup as shown in Fig. 2(a). The polarization properties of light emerging from the endoscope when illuminated with linearly polarized light between 0 and 180 deg are presented in Figs. 2(b) and 2(c).

Figure 2(b) presents the measured degree of linear polarization, degree of circular polarization, and degree of polarization (DOP) of the light exiting the endoscope. As light is transmitted through the endoscope, the degree of linear polarization drops to around 80% and the circular polarization increases equally. Hence, the DOP remains around 1, which indicates that there are very low optical losses, scattering events, and sources of depolarization in the endoscope. We believe that the introduction of elliptically polarized light in the endoscope is probably due to retarders that are placed inside the probe. Once the retardance of the endoscope is known, calibration routines can provide the correct input Stokes vector.[33] Furthermore, Fig. 2(c) represents the angle of polarization of the output Stokes vector that is not affected by the optical elements of the endoscope.

3.3 *Targeting Adenomatous Tumor and Dysplasia in Azoxymethane-Dextran Sodium Sulfate Tissue Sections with NIR Fluorescent Dye-Labeled Octapeptide (LS301)*

Some colon lesions lie below the mucosa, requiring imagining techniques with depths beyond a few millimeters. Capitalizing on the ability of NIR light to penetrate deeper into tissue with low background autofluorescence compared to visible light, we used a NIR fluorescent dye-labeled octapeptide, LS301; see Figs. 3(a) and 3(b), which has been shown to selectively accumulate in malignant tumors.[22] We explored the feasibility of using LS301 to detect inflammation-driven colon carcinogenesis using the clinically relevant AOM-DSS murine model. Precancerous and cancerous lesions from AOM-DSS mouse colons were identified and sectioned before incubation with LS301, and the slides were imaged by fluorescence microscopy. Figure 3(c) demonstrates that LS301 uptake was highly specific for adenomatous tumor, with minimal fluorescence from the

surrounding uninvolved regions. The contrast between adenomatous tumor and surrounding uninvolved tissue was 56 ± 9 (standard error of the mean, SEM was used in this study) with an average contrast-to-noise-ratio (CNR) of 7 ± 1.13. This impressive level of specificity of LS301 was maintained when evaluating tissues exhibiting features sensitive to precancerous lesions, such as the aberrant crypt foci as illustrated in Fig. 3(d). For example, the contrast between dysplastic lesions and the surrounding uninvolved regions as shown in Fig. 3(e) was 37.4 ± 3.6 with an average CNR of 8.72 ± 0.88. In contrast, the dye cypate alone did not show any selective uptake in the colon lesions. Therefore, we used LS301 for subsequent *in vivo* studies of the AOM-DSS model.

3.4 *In Vivo Fluorescence and Polarization Endoscopy*

3.4.1 *Near-infrared fluorescence endoscopy utilizing novel topical administration method in azoxymethane-dextran sodium sulfate and wound-healing models*

Having demonstrated the feasibility of detecting CAC and dysplasia by fluorescence imaging and established the polarization contrast between diseased and normal tissues, we next assessed the use of these combined techniques for *in vivo* imaging. Previous small animal imaging of tumors with LS301 have relied on the intravenous administration of the molecular probe.[22] Typically, a wait time of 24 h is needed to obtain excellent contrast between tumors and uninvolved surrounding tissues. While this imaging time point is acceptable for many clinical applications, a fast-acting approach would be preferred for colonoscopy. Toward this goal, we explored a topical delivery method in which the molecular probe is sprayed on the colon during screening endoscopy. We found that poloxamer (Pluronic F127), which is approved for human use, can solubilize LS301 [see Fig. 1(b); Methods, Formulation of LS301]. More importantly, the formulation undergoes a reversible thermoresponsive sol-gel transition, with a critical transition temperature of 20°C. This previously unexplored topical application of NIR molecular probes allowed endoscope-mediated spraying of the cold formulation, resulting in a rapidly formed thin layer of gel around the colon tissue. With this method, we observed a mean CNR of 20.64 ± 1.65 between the adenomatous tumor and the surrounding uninvolved tissue, and 12.1 ± 1.03 between flat lesions and the surrounding uninvolved regions as displayed in Figs. 5(a) and 6(a), respectively. These outcomes represent a six-fold and three-fold increase in mean fluorescence intensity from the adenomatous tumor and flat lesions, respectively, relative to the surrounding uninvolved tissues.

Inflamed tissues generally retain optical contrast agents by several mechanisms, including nonspecific retention or entrapment by activated macrophages. Peyer's patches are the sites of the host defense system where macrophages, dendritic cells, B-lymphocytes, and T-lymphocytes reside. We observed that LS301 did not accumulate in Peyer's patches in the mucosa as shown by Fig. 6(c). The lack of LS301 fluorescence in this tissue indicates the high selectivity of the imaging agent for cancer-associated lesions. To further assess the feasibility of distinguishing wound-repair associated inflammation from colon cancer and dysplasia, we induced colon injury in mice by removing single full thickness areas of the mucosa and submucosa using a flexible biopsy needle. The leading edge of the injured epithelium is known to form cables of actin filaments
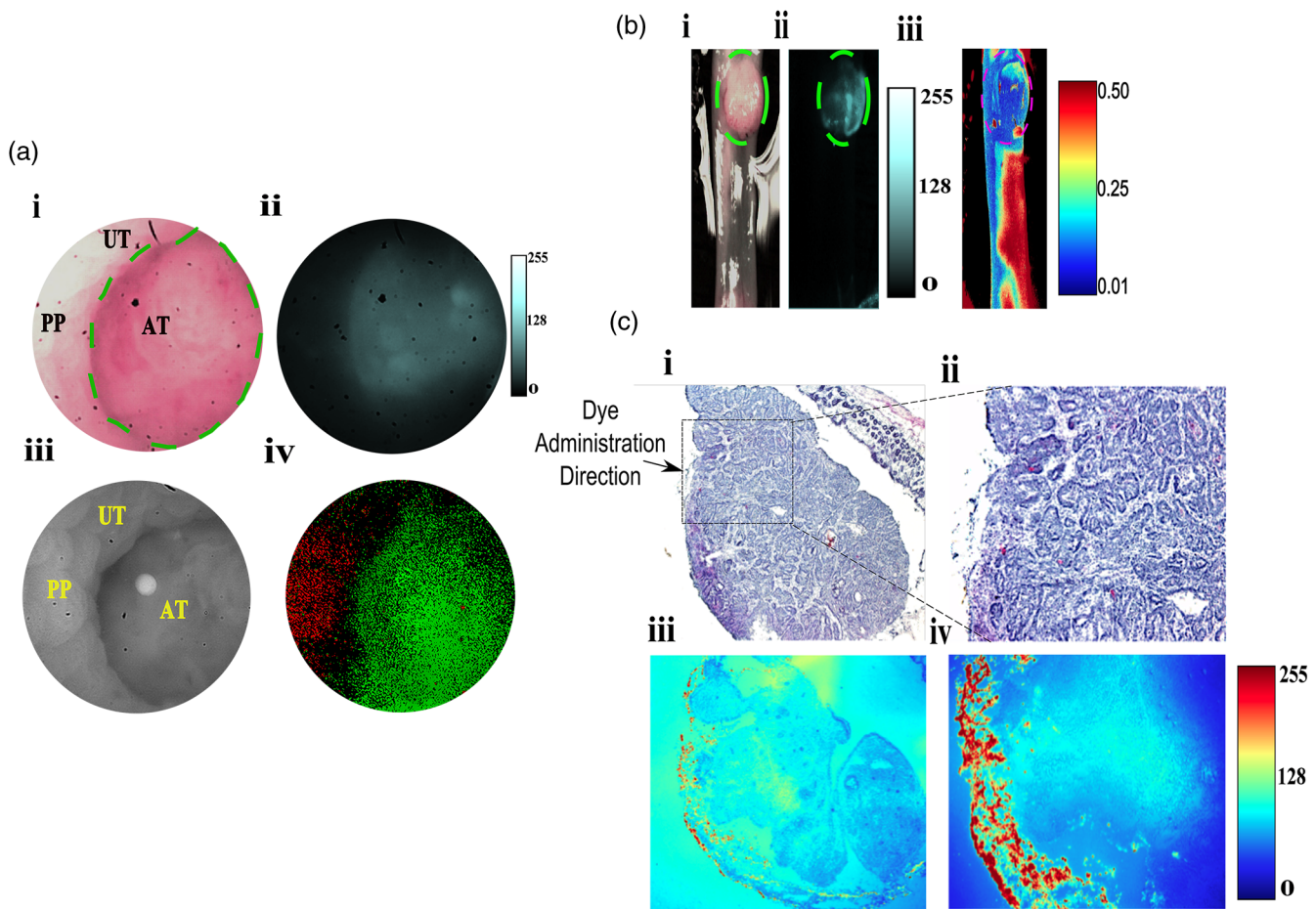
Fig. 5 *In vivo* and *in situ* fluorescence and polarization endoscopy of adenomatous tumor-surrounding uninvolved boundary. (a) *In vivo* fluorescence and polarization endoscopy. (i) RGB color image of the tumor identified in the distal colon of an AOM-DSS treated mouse. (ii) Fluorescence image clearly identifies boundaries of the tumor. (iii) Grayscale image consisting of DoLP and AOP information in the polarization mode at 30 fps. Bright spot in image is from the light source. (iv) Thresholded DoLP mask image identifies inflamed regions (reported as DoLP value above 10%; red color) and cancerous regions (DoLP value under 5%; green color). (b) *Ex-vivo* (i) RGB, (ii) NIR fluorescence, and (iii) polarization images of tumor identified in (a). Dotted yellow lines in (i) and (ii) indicate the boundary of the tumor. Thresholded DoLP mask image identifies cancerous regions (DoLP value under 10%; green color). (c) Histological validation of adenomatous tumor identified in (b), along with corresponding NIR fluorescence intensity. Dotted rectangle identifies the region under investigation in (ii and iv). Arrow indicates the direction of molecular probe administration. UT: uninvolved tissue, PP: Peyer's patch, AT: adenomatous tumor.

extending from cell to cell, forming a ring around the wound circumference and facilitating wound closure.[34] Topical administration of LS301 resulted in a barely detectable mean CNR of 1.62 ± 0.41 between the inflamed regions and surrounding uninvolved regions in this wound-healing model using our current fluorescence endoscope as shown in Fig. 7. *Ex-vivo* sections of exteriorized colon from the tumor and inflamed regions were examined as shown in Figs. 5(b) and 6(b). Consistent with *in vivo* results, identified adenomatous tumor and flat lesions showed high fluorescence intensity as seen in Figs. 5(c) and 6(c). A graded fluorescence intensity pattern was observed within the adenomatous tumor mass as shown in Fig. 5(c), illustrating the diffusion and retention of LS301 in the lesions within 10 min of administration. LS301 also showed high specificity toward dysplastic lesions possessing features such as aberrant crypt foci as shown in Fig. 6(c). Figure 7(a) demonstrates minimal fluorescence in the lumen of colonic crypts and features of inflammation, such as regions of neutrophil activation. H&E

staining confirmed the presence of these morphological features as shown in Figs. 7(c) and 7(d). *Ex vivo* studies relatively demonstrated higher fluorescence intensities from regions exhibiting higher epithelial proliferation, which is a consequence of wound repair as shown in Fig. 7(c).

3.4.2 *Polarization endoscopy utilizing degree of linear polarization contrast in azoxymethane-dextran sodium sulfate and wound healing inflammation models*

The fluorescence molecular imaging approach deployed above does possess certain limitations. It does not furnish structural information that is useful for validating the presence of cancer or dysplasia; hence, this information must be obtained via *ex vivo* histologic validation. *Ex vivo* histology requires tissue biopsy and offline analysis that could delay clinical decisions and result in repeat hospital visits. Although the molecular
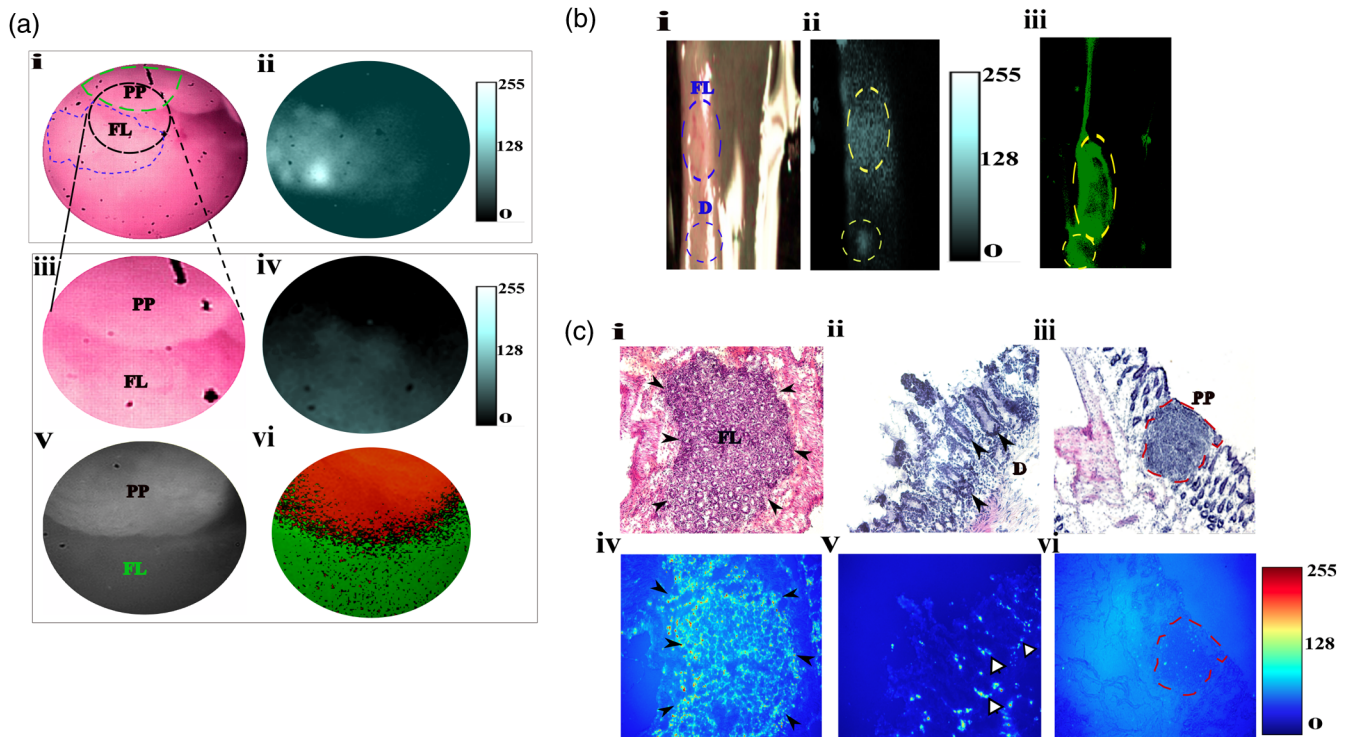
Fig. 6 *In vivo* and *ex vivo* fluorescence and polarization endoscopy of flat lesion-surrounding uninvolved boundary. (a) *In vivo* fluorescence and polarization endoscopy. (i) RGB color image of the flat lesion identified in the distal colon of an AOM-DSS treated mouse. Dotted green line outlines the boundary of the Peyer's patch. Dotted blue line outlines the boundary of the flat lesion biopsied in accordance to corresponding fluorescence image. Dotted black circle identifies the region that was investigated more closely (iii) and serves as the field-of-view (FOV) region for the remaining *in vivo* images. Grayscale image consisting of DoLP and AOP information in the polarization mode at 30 fps. (v) Corresponding region to (iii) identified by polarization camera in grayscale. (vi) Thresholded DoLP mask image identifies Peyer's patch (reported as DoLP value above 10%; red color) and flat lesion (reported as DoLP value less than 5%; green color). (b) *Ex-vivo* RGB (i), NIR fluorescence (ii), and DOLP (iii) images of flat lesion identified in (a). Dotted blue line indicates the boundary of the flat lesion (FL) and dysplastic tissue (d). (ii) Corresponding NIR fluorescence image demonstrates fluorescence signal from flat lesions and dysplastic tissue. (iii) Dotted red lines indicate the corresponding flat lesion and dysplastic tissue. Thresholded DoLP mask image identifies cancerous regions (DoLP value under 10%; green color) (c) Histological validation of flat lesion, dysplastic tissue, and Peyer's patch identified in (a) and (b) along with corresponding NIR fluorescence intensity, respectively. For the flat lesion, black solid arrows indicate the boundary of tumor in the H&E and NIR fluorescence images. For dysplastic tissue, black solid arrows indicate the aberrant crypts identified by LS301 in the H&E image and white solid arrows in the NIR fluorescence image. A dotted red line indicates the boundary of the Peyer's patch in the H&E and NIR fluorescence images. PP: Peyer's patch, FL: flat lesion.

fluorescence method can distinguish inflamed from cancerous tissue or flat lesions, a complementary method that can instantly validate the negative fluorescence contrast in suspicious, but noncancerous tissues would facilitate rapid clinical decision making during colonoscopy. Finally, the topical application of fluorescence molecular probes and the subsequent washing step occasionally leave residual dye and gel in the vicinity of uninvolved tissue, which could be misinterpreted as cancerous. To resist oversampling of the colon through purely fluorescence guided biopsies and to provide real-time confirmation of suspicious lesions, we incorporated the DoLP contrast obtained from reflectance polarization imaging into our fluorescence endoscope. Both the fluorescence and DoLP contrasts are orthogonal, providing complementary positive fluorescence and DoLP signals in cancerous and uninvolved colon tissues, respectively, but negative fluorescence and DoLP signals in uninvolved and cancerous colon tissues, respectively. To rule out a false positive DoLP signature caused by the irregular contours of the colon, a small FOV was used to interrogate tissue highlighted by molecular fluorescence imaging.

Postacquisition, regions of interest were selected to quantify the DoLP signature as shown in Fig. 8. For adenomatous polyps, a mean DoLP value of 0.0414 ± 0.0142 was obtained compared to 0.0816 ± 0.0173 from the surrounding uninvolved regions. We found a similar trend for flat lesions, with a mean DoLP of 0.0225 ± 0.0073 compared to 0.0924 ± 0.0284 from the surrounding wall as shown in Fig. 9. While the fluorescence imaging was able to detect pathologic tissue, the high DoLP signal in uninvolved tissue provides an anatomical landscape of the colon and identifies different types of uninvolved colon tissue. For example, Peyer's patches, which were not detected by fluorescence, had a high mean DoLP signal of 0.1064 ± 0.0104, compared to 0.0872 ± 0.022 from the surrounding wall (Fig. 8). These differences in DoLP signal are probably due to the higher structural integrity of Peyer's patches caused by the high density of lymphoid tissue. In the
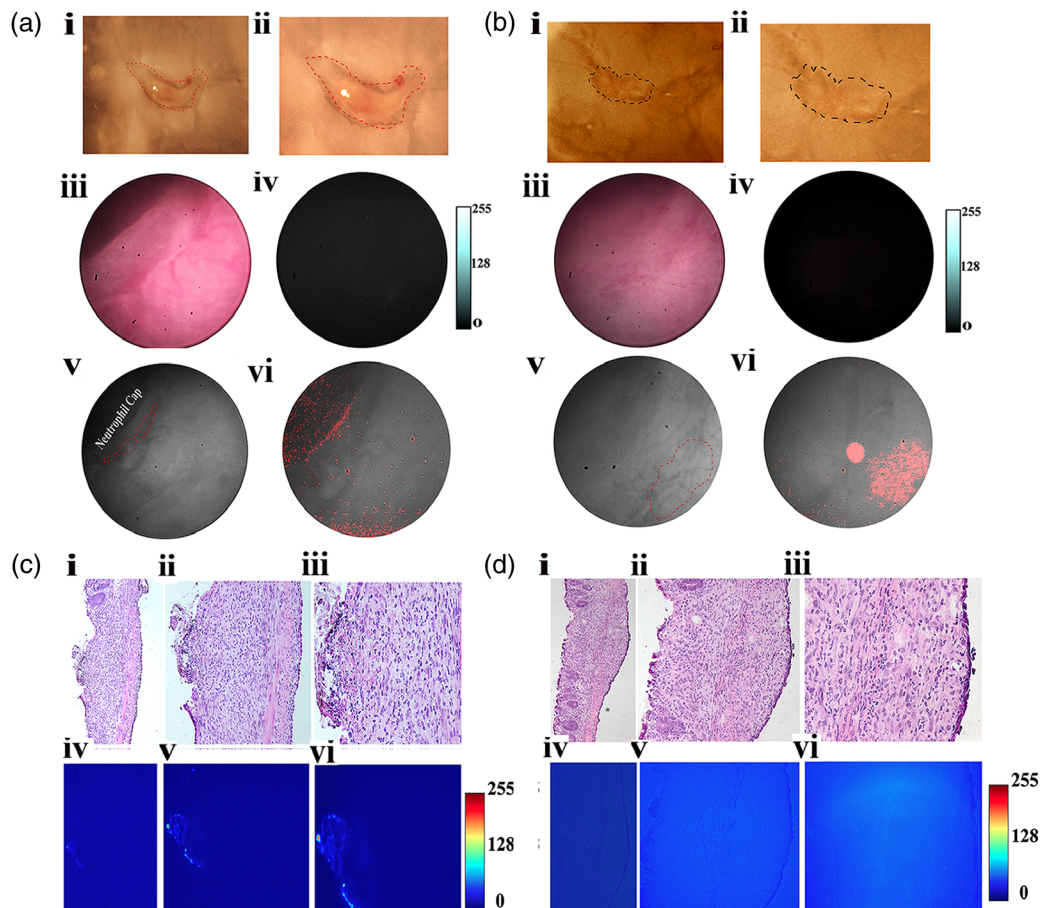
Fig. 7 *In vivo* and *ex vivo* fluorescence and polarization endoscopy of wound healing inflammation model. (a) *Ex vivo* brightfield images of wounds created via endoscopy procedure *in vivo*. (i,ii) Wound bed at day 4 postendoscopic injury. Dotted red line marks the neutrophil cap formed as a result of inflammation. (iii) RGB color image of the corresponding wound bed identified in (i) within the distal colon of an injury mouse. (iv) Corresponding NIR fluorescence image demonstrates very minimal binding of the probe toward the proliferative cells in the neutrophil cap. (v) Grayscale image captured using the polarization camera. Dotted red line marks the neutrophil cap region. (vi) Corresponding thresholded DoLP mask image identifying regions higher than established value of 10.6%. (b) *Ex vivo* brightfield images of wounds created via endoscopy procedure *in vivo*. (i,ii) Wound bed at day 4 postendoscopic injury. Dotted red line marks the boundary of the wound bed. (iii) RGB color image of the corresponding wound bed identified in (i) within the distal colon of an injury mouse. (iv) Corresponding NIR fluorescence image demonstrates minimal binding of the probe toward the wound bed (v) Grayscale image captured using the polarization camera. Dotted red line marks the boundary of the wound bed. (vi) Corresponding, thresholded DoLP mask image identifying regions higher than established value of 10.6%. (c) *Ex vivo* fluorescence binding pattern and histologic validation. (i,ii,iii) H&E images of disrupted epithelium in the inflamed wound region identified in (a). (iv,v,vi) Corresponding NIR fluorescence microscopy images identify proliferative cells in the wound bed. (d) *Ex vivo* fluorescence binding pattern and histology validation. (i,ii,iii) H&E images of wound bed in (a). (iv,v,vi) Corresponding NIR fluorescence microscopy images identify proliferative cells in the wound bed.

wound-healing model, the increase in newly formed actin filaments resulted in a high birefringence signal, thereby polarizing the incident light in the process.[35] For example, a high mean DoLP signal of 0.1363 ± 0.0379 was obtained along the epithelium surrounding the wound bed as demonstrated in Figs. 7(a) and 7(b). Thus, the combined high polarization and low LS301 fluorescence signals in nontumor tissue provide real-time validation of suspicious lesions during endoscopy, which reduces the number of false positives and unnecessary biopsies.

To examine colon tissue under controlled conditions and to provide maximum contrast, *ex-vivo* polarization imaging was conducted at 35 deg using the tissue from the *in vivo* study.

Consistent with the *in vivo* studies, Fig. 6(b) exhibits a lower DoLP signature that was obtained for flat lesions compared to the surrounding uninvolved regions. Patches of higher DoLP signature were observed around the flat lesion, clearly identifying the nontumor Peyer's patch.

4 Discussion

We have developed an integrated fluorescence and polarization endoscope for detecting and providing real-time confirmation of CAC, dysplasia, and associated flat lesions that are difficult to detect without *ex vivo* histologic validation. Although depressed cancerous lesions and sessile serrated adenomas have different pathologies, we used the term flat lesions for both flat depressed
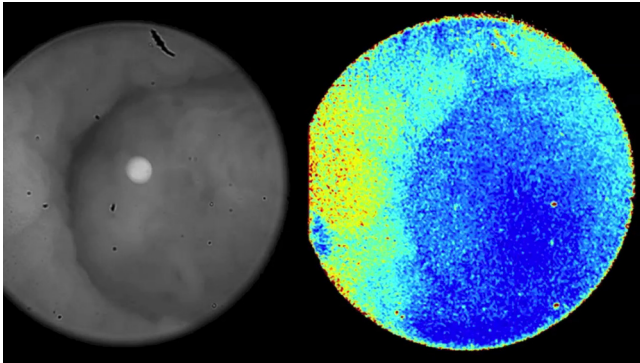
Fig. 8 *In vivo* polarization endoscopy of an adenomatous tumor in an AOM-DSS treated mouse (raw images). *In vivo* imaging provides (A) grayscale, and (B) DoLP at 30 fps. Dotted black lines represent image segmentation masks used for quantification of DoLP signal. Masks identify inflammation (I), tumor (T), and uninvolved surrounding tissue (U). Regions in the image that were verified via histology. UT: Uninvolved Tissue, PP: Peyer's patch, AT: Adenomatous Tumor (MOV, 19.3 MB) [URL: http://dx.doi.org/10.1117/1.JBO.19.12.126002.1].
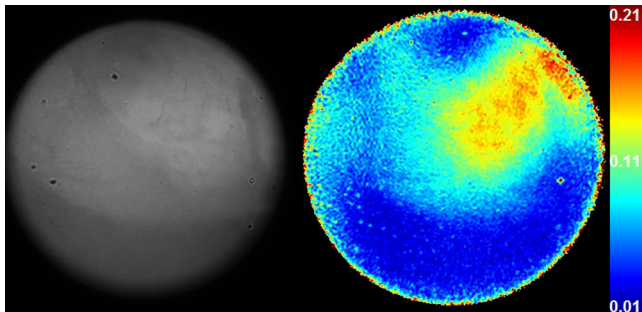

Fig. 9 *In vivo* and *ex vivo* polarization endoscopy of a flat lesion identified in an AOM-DSS treated mouse (raw images). *In vivo* imaging provides (A) grayscale, and (B) DoLP, at 30 fps. Dotted yellow and red lines mark the corresponding flat lesion in each image (MOV, 13.2 MB) [URL: http://dx.doi.org/10.1117/1.JBO.19.12.126002.2].

carcinomas and adenomas to reflect the similarity in the level of difficulty in detecting these lesions during conventional colonoscopy. Unlike current endoscopic techniques that interrogate molecular or structural signatures of CAC and dysplasia, the combined fluorescence and polarization contrasts create a new paradigm for identifying colonic lesions with high accuracy. The murine AOM-DSS model used in this study recapitulates the molecular pathways and morphological features of CAC from dysplasia to carcinoma.[36] Similarly, the murine wound-healing model exhibits key features of inflammation that are reminiscent of malignancy. These include wound-associated epithelial cell proliferation and stromal neutrophil and macrophage recruitment in the wound bed.

Our fluorescence imaging approach is similar to chromoendoscopy, where nontumor targeted dyes are topically applied for improved visualization of dysplastic lesions.[11,37] Previous studies attempted to use the FDA-approved NIR dye, indocyanine green (ICG), to enhance the detection of submucosal colon lesions, and to minimize the tissue autofluorescence.[38] Unfortunately, the high background ICG fluorescence in the subserosa around the tumor confounded data analysis. In a

recent study, we showed that LS301 selectively accumulates in tumors and achieves high tumor-to-background fluorescence at 24-h post intravenous injection.[22] Using the AOM-DSS treated mouse model of CAC, we demonstrated in this study that *ex-vivo* staining of colon tissue with LS301 successfully identified adenomatous tumors and dysplastic lesions in the colon tissue as shown in Figs. 3(c) and 3(d). *Ex vivo* histologic validation confirmed the *in vivo* imaging analysis. These results demonstrate that molecular fluorescence endoscopy, aided by LS301, detects multiple stages of oncogenesis with a high potential to improve the management of colorectal cancer.

However, the intravenous administration of LS301 and the long wait time (24 h) to achieve high fluorescence contrast between tumors and uninvolved surrounding colon tissue are not suitable for colonoscopy. In addition, the excretion of LS301 through the hepatobiliary pathway after intravenous injection increases background NIR fluorescence in the colon, compounding the detection of flat lesions and dysplasia. Based on our *ex vivo* study, we postulated that the rapid and prolonged retention of LS301 in pathologic tissues lends it to topical administration during colonoscopy. The results demonstrate that the formulation of LS301 in a poloxamer sol-gel transition system allowed us to topically administer the imaging agent with a spray catheter during endoscopy. In contrast to the use of generic dyes for chromoendoscopy, the selective uptake of LS301 in CAC and dysplastic colon tissue minimized nonspecific uptake in uninvolved mucosa, ushering in a new procedure for topical administration of tumor-targeted molecular probes. The commercially available poloxamer not only improved the solubility of the hydrophobic LS301, but also aided in the uniform coating of the tissue, thereby increasing the interaction of the molecular probe gel formulation with the colon tissue under investigation. The observed high mean CNR obtained from adenomatous tumors and flat lesions compared to surrounding uninvolved tissue is a function of the improved molecular probe selectivity for tumors, reduced autofluorescence in the NIR imaging window, and enhanced incubation time provided by the sol-gel formulation. This sol-gel approach can be extended to previously reported methods for imaging colon cancer and dysplasia. These include Cy5.5 labeled cathepsin B substrate used to identify polyps in adenomatous polyposis coli (Apc min) mice[39] and fluorescein-labeled VRPMPLQ heptapeptide that was shown to preferentially bind dysplastic rather than normal mucosa.[19] Unlike these molecular probes which are confined to identifying only specific stages of tumorigenesis,[40,41] LS301 uniquely captures multiple stages of cancer development. A limitation of the sol-gel method is the lag time between topical application and imaging. Our current protocol uses about 10 min to optimize tumor uptake. A future goal is to optimize the procedure to shorten the incubation time for rapid assessment of the colon.

Although the topical administration of LS301 has enormous benefits for screening endoscopy, we found that polarization contrast can provide real-time cross-validation of suspicious lesions with an orthogonal but complementary signal. This approach is expected to minimize the need for *ex vivo* biopsy, to accelerate the medical decisions, and to improve the clinical outcomes with minimal recall rates. In addition, false-positive fluorescence arising from residual gelatinous materials in healthy colon can readily be identified by the low polarization contrast in healthy tissue.

Previous studies have reported the use of polarized light scattering spectroscopy and reflectance spectroscopy for tissue analysis.[27,42,43] In these studies, *ex vivo* colonic tissue specimens were illuminated with polarized light and morphological maps of the specimens were constructed based on varying nuclear sizes, population density, and refractive index.[27,42,43] However, the system configuration and challenges in real-time mapping of the polarization signal undermine their use for *in vivo* applications. We circumvented these challenges by developing an imaging configuration and sensor setup capable of reporting DoLP and AOP changes in the reflected light, while taking the relative positions of the camera with respect to the tissue into account. As DoLP reports on the fraction of reflected light that is linearly polarized, we expect differences between the DoLP signature in epithelial layer of diseased and healthy tissues. Precancerous and cancerous lesions within the epithelial layer possess distinct morphological features, such as increased nuclear size and increased nuclear-cytoplasmic ratio, which result in significant multiple scattered components of light and a corresponding decrease in DoLP signature. A mean DoLP change of 4% was obtained for polypoid tissue in the surrounding uninvolved region. This change was validated by simulation results as depicted in Fig. 4(b), where we predicted a change of 4% in DoLP signature when imaging at 15 deg. In the case of flat lesions, we obtained a DoLP difference of 7% relative to the surrounding Peyer's patch regions. The exceptionally high DoLP signal in Peyer's patches stems from the formation of firmly matted fibrotic bands within the serosa and mesentery as shown in Fig. 8. The increase in concentration of linearly birefringent material, such as actin, results in a DoLP difference of 10% in the inflamed regions compared to the surrounding uninvolved colonic tissue. We demonstrated our ability to rapidly interrogate regions of interest in real time (at 40 fps) without distortion from motion artifacts arising from respiration and peristalsis as shown in Figs. 8 and 9.

In summary, the combination of a tumor-targeting molecular probe, topical application of a contrast agent with a biocompatible sol-gel formulation, and the development of a multimodal color, NIR fluorescence, and polarization endoscope provides a new paradigm for the accurate detection of colonic lesions, including CAC, dysplasia, and the associated flat lesions. An extension of this approach to a wound-healing inflammation model[44] demonstrated a reversal of the fluorescence-polarization signal, highlighting the complementary nature of both techniques. The ease of incorporating both fluorescence and polarization fibers into an existing endoscope allows seamless integration into current screening colonoscopy protocols. A similar approach can be envisaged for other forms of epithelial cancer such as esophageal, cervical, bladder, skin, and stomach tumors that account for over 65% of the noncolorectal cancer deaths.

Acknowledgments

References

1. J. A. Eaden et al., "The risk of colorectal cancer in ulcerative colitis: a meta-analysis," *Gut* **48**(4), 526–535 (2001).
2. N. A. Molodecky et al., "Increasing incidence and prevalence of the inflammatory bowel diseases with time, based on systematic review," *Gastroenterology* **142**(1), 46–54 (2012).
3. R. Siegel et al., "Cancer statistics, 2012," *Ca–Cancer J. Clini.* **62**(1), 10–29 (2012).
4. S. D. Markowitz et al., "Molecular origins of cancer: molecular basis of colorectal cancer," *N. Engl. J. Med.* **361**(25), 2449–2460 (2009).
5. S. H. Itzkowitz et al., "Inflammation and cancer IV. Colorectal cancer in inflammatory bowel disease: the role of inflammation," *Am. J. Physiol. Gastrointest. Liver Physiol.* **287**(1), G7–G17 (2004).
6. R. Kiesslich et al., "Methylene blue-aided chromoendoscopy for the detection of intraepithelial neoplasia and colon cancer in ulcerative colitis," *Gastroenterology* **124**(4), 880–888 (2003).
7. T. Ullman et al., "Progression of flat low-grade dysplasia to advanced neoplasia in patients with ulcerative colitis," *Gastroenterology* **125**(5), 1311–1319 (2003).
8. M. Kanneganti et al., "Animal models of colitis-associated carcinogenesis," *J. Biomed. Biotechnol.* **2011**, 342637 (2011).
9. C. Neufert et al., "An inducible mouse model of colon carcinogenesis for the analysis of sporadic and inflammation-driven tumor progression," *Nat. Protoc.* **2**(8), 1998–2004 (2007).
10. F. A. Farraye et al., "AGA technical review on the diagnosis and management of colorectal neoplasia in inflammatory bowel disease," *Gastroenterology* **138**(2), 746–774 (2010).
11. M. F. Neurath et al., "Is chromoendoscopy the new standard for cancer surveillance in patients with ulcerative colitis?," *Nat. Clin. Pract. Gastroenterol. Hepatol.* **6**(3), 134–135 (2009).
12. A. Hoffman et al., "High definition colonoscopy combined with i-Scan is superior in the detection of colorectal neoplasias compared with standard video colonoscopy: a prospective randomized controlled trial," *Endoscopy* **42**(10), 827–833 (2010).
13. C. Becker et al., "High resolution colonoscopy in live mice," *Nat. Protoc.* **1**(6), 2900–2904 (2007).
14. F. Emura et al., "Narrow-band imaging optical chromocolonoscopy: advantages and limitations," *World J. Gastroenterol.* **14**(31), 4867–4872 (2008).
15. J. Pohl et al., "Pancolonic chromoendoscopy with indigo carmine versus standard colonoscopy for detection of neoplastic lesions: a randomised two-centre trial," *Gut* **60**(4), 485–490 (2011).
16. P. A. Testoni et al., "Optical coherence tomography in detection of dysplasia and cancer of the gastrointestinal tract and bilio-pancreatic ductal system," *World J. Gastroenterol.* **14**(42), 6444–6452 (2008).
17. E. Zagaynova et al., "Endoscopic OCT with forward-looking probe: clinical studies in urology and gastroenterology," *J. Biophoton.* **1**(2), 114–128 (2008).
18. S. Foersch et al., "Molecular imaging of VEGF in gastrointestinal cancer in vivo using confocal laser endomicroscopy," *Gut* **59**(8), 1046–1055 (2010).
19. P. L. Hsiung et al., "Detection of colonic dysplasia in vivo using a targeted heptapeptide and confocal microendoscopy," *Nat. Med.* **14**(4), 454–458 (2008).
20. H. Neumann et al., "Confocal laser endomicroscopy: technical advances and clinical applications," *Gastroenterology* **139**(2), 388–392 (2010).
21. T. York et al., "Characterization of a visible spectrum division-of-focal-plane polarimeter," *Appl. Opt.* **51**(22), 5392–5400 (2012).
22. Y. Liu et al., "Hands-free, wireless goggles for near-infrared fluorescence and real-time image-guided surgery," *Surgery* **149**(5), 689–698 (2011).
23. S. Achilefu et al., "Synthesis, in vitro receptor binding, and in vivo evaluation of fluorescein and carbocyanine peptide-based optical contrast agents," *J. Med. Chem.* **45**(10), 2003–2015 (2002).
24. T. Valery, *Tissue Optics: Light Scattering Methods and Instruments for Medical Diagnosis*, SPIE Press, Bellingham, Washington (2000).
25. D. Hidovic-Rowe et al., "Modelling and validation of spectral reflectance for the colon," *Phys. Med. Biol.* **50**(6), 1071–1093 (2005).
26. J. Ramella-Roman et al., "Three Monte Carlo programs of polarized light transport into scattering media: part I," *Opt. Express* **13**(12), 4420–4438 (2005).

27. V. Backman et al., "Detection of preinvasive cancer cells," *Nature* **406**(6791), 35–36 (2000).
28. R. S. Gurjar et al., "Imaging human epithelial properties with polarized light-scattering spectroscopy," *Nat. Med.* **7**(11), 1245–1248 (2001).
29. L. T. Perelman, "Observation of periodic fine structure in reflectance from biological tissue: a new technique for measuring nuclear size distribution," *Phys. Rev. Lett.* **80**(627–630 (1998).
30. H. Ao et al., "Thermal coagulation-induced changes of the optical properties of normal and adenomatous human colon tissues in vitro in the spectral range 400–1,100 nm," *Phys. Med. Biol.* **53**(8), 2197–2206 (2008).
31. V. Gruev et al., "CCD polarization imaging sensor with aluminum nanowire optical filters," *Opt. Express* **18**(18), 19087–19094 (2010).
32. Y. Liu et al., "Complementary fluorescence-polarization microscopy using division-of-focal-plane polarization imaging sensor," *J. Biomed. Opt.* **17**(11), 116001 (2012).
33. S. B. Powell et al., "Calibration methods for division-of-focal-plane polarimeters," *Opt. Express* **21**(18), 21039–21055 (2013).
34. Y. Danjo and I. K. Gipson, "Actin 'purse string' filaments are anchored by E-cadherin-mediated adherens junctions at the leading edge of the epithelial wound, providing coordinated cell movement," *J. Cell Sci.* **111**(22), 3323–3332 (1998).
35. K. Katoh et al., "Birefringence imaging directly reveals architectural dynamics of filamentous actin in living growth cones," *Mol. Biol. Cell* **10**(1), 197–210 (1999).
36. T. A. Ullman et al., "Intestinal inflammation and cancer," *Gastroenterology* **140**(6), 1807–1816 (2011).
37. R. Kiesslich et al., "Surveillance colonoscopy in ulcerative colitis: magnifying chromoendoscopy in the spotlight," *Gut* **53**(2), 165–167 (2004).
38. M. Kusano et al., "Sentinel node mapping guided by indocyanine green fluorescence imaging: a new method for sentinel node navigation surgery in gastrointestinal cancer," *Dig. Surg.* **25**(2), 103–108 (2008).
39. K. Marten et al., "Detection of dysplastic intestinal adenomas using enzyme-sensing molecular beacons in mice," *Gastroenterology* **122**(2), 406–414 (2002).
40. M. Karin et al., "NF-kappaB: linking inflammation and immunity to cancer development and progression," *Nat. Rev. Immunol.* **5**(10), 749–759 (2005).
41. S. I. Grivennikov et al., "Immunity, inflammation, and cancer," *Cell* **140**(6), 883–899 (2010).
42. M. B. Wallace et al., "Endoscopic detection of dysplasia in patients with Barrett's esophagus using light-scattering spectroscopy," *Gastroenterology* **119**(3), 677–682 (2000).
43. K. Sokolov et al., "Reflectance spectroscopy with polarized light: is it sensitive to cellular and nuclear morphology," *Opt. Express* **5**(13), 302–317 (1999).
44. H. Seno et al., "Efficient colonic mucosal wound repair requires Trem2 signaling," *Proc. Natl. Acad. Sci. U. S. A.* **106**(1), 256–261 (2009).

Tauseef Charanya is a biomedical engineering graduate student at Washington University in St. Louis. He received his BS degree in biomedical engineering from Texas A&M University in 2010. His research interests include endoscopy, surgical margin assessment tools, and fluorescence and polarization microscopy methods. He is a member and serves as the president of the WU Chapter of SPIE.

Timothy York is a PhD candidate in computer engineering at Washington University in St. Louis. He received his B.S.E.E. and M.S.E.E degrees from Southern Illinois University Edwardsville in 2002 and 2007, respectively. He worked as a computer engineer for the United States Air Force from 2006 to 2009. His current work focuses on polarization image sensors and their applications, especially in the field of biomedical imaging. He is a member of SPIE and IEEE.

Sharon Bloch is a senior scientist at Washington University School of Medicine. She received her PhD degree in cell and molecular biology from Saint Louis University, where she studied bone remodeling. Her research interests include regulation of differential gene expression and molecular imaging techniques.

Gail Sudlow is a research assistant since 2008 at Washington University in St. Louis. She received her BS degree in biology from South Dakota State University. Her professional skills include cell culture, animal modeling, *in vivo* animal imaging, histology, immunohistochemistry, and fluorescence microscopy. She also serves as the lab manager.

Kexian Liang is a senior research technician at Washington University in St. Louis. She holds a BS degree in chemistry. Her professional skills include peptide synthesis, as well as conjugation and analytical chemistry.

Missael Garcia is a computer engineering graduate student at Washington University in St. Louis. He received his MS degree in electrical engineering from SIUE in 2013 and his BS degree in mechatronics engineering from ITESM in 2012. His research interests include imaging sensors, polarization optics characterization, and polarization applications such as three-dimensional (3-D) reconstruction.

Walter J. Akers is assistant professor of radiology. He combines his experience as a veterinarian and biological engineer to develop novel optical and multimodal molecular imaging approaches to diagnose, stage, and monitor disease processes through detection of molecular events in living systems and to translate optical imaging methods to clinical applications in human medicine.

Deborah Rubin is professor of medicine and developmental biology in the Division of Gastroenterology at Washington University School of Medicine. She is the director of the Advanced Imaging and Tissue Analysis Core of Wash U.'s Digestive Diseases Research Core Center, and chair of the MA/MD Program for Medical Student Research. She is a fellow of the American Gastroenterological Association. Her research interests include regulation of epithelial regeneration and stem cell therapy of short bowel syndrome, and epithelial-mesenchymal interactions in colitis and colitis associated cancer.

Viktor Gruev received his MS and PhD degrees in electrical and computer engineering from Johns Hopkins University, Baltimore, MD, USA, in May 2000 and September 2004, respectively. After finishing his doctoral studies, he was a postdoctoral researcher at the University of Pennsylvania, Philadelphia, PA, USA. Currently, he is an associate professor in the Department of Computer Science and Engineering, Washington University in St. Louis, St. Louis, MO, USA. His research interests include imaging sensors, polarization imaging, bioinspired circuits and optics, biomedical imaging, and micro/nanofabrication.

Samuel Achilefu, PhD, is a professor of radiology, biomedical engineering, and biochemistry and molecular biophysics. He serves as the chief of Optical Radiology Laboratories, director of Washington University Molecular Imaging Program, co-leader of the Oncologic Imaging Program of the Siteman Cancer Center, and editor-in-chief of *Current Analytical Chemistry*. His research interests include the development of molecular imaging probes and therapeutic molecules, and new methods and devices for biomedical applications. He is a fellow of SPIE.